World Journal of Engineering and Technology, 2026, 14(4), 1018-1031
https://www.scirp.org/journal/wjet
ISSN Online: 2331-4249
ISSN Print: 2331-4222

# Study on Structural Parameter Optimization of a Spring-Loaded Casing Scraper

**Song Zeng[1], Chaoyang Yu[2*], Geng Peng[1], Zheng Li[1]**

[1]Oil and Gas Technology Research Institute of PetroChina Southwest Oil & Gas Field Company, Chengdu, China
[2]School of Mechatronic Engineering, Southwest Petroleum University, Chengdu, China
Email: *17760596339@163.com

**How to cite this paper:** Zeng, S., Yu, C.Y., Peng, G. and Li, Z. (2026) Study on Structural Parameter Optimization of a Spring-Loaded Casing Scraper. *World Journal of Engineering and Technology*, **14**, 1018-1031.
https://doi.org/10.4236/wjet.2026.144061

**Received:** September 20, 2026
**Accepted:** October 31, 2026
**Published:** November 3, 2026

Copyright © 2026 by author(s) and Scientific Research Publishing Inc.
This work is licensed under the Creative Commons Attribution International License (CC BY 4.0).
http://creativecommons.org/licenses/by/4.0/
Open Access

## Abstract

When cement attachments on the casing inner wall are removed, thick continuous cement rings can sharply increase scraping resistance and cumulative work, and may even suspend the operation. To address this problem, a 7-inch spring-loaded casing scraper was studied through blade spring compression tests, casing obstacle-removal bench tests, and finite element orthogonal design. The equivalent stiffness of the spring assembly on a single blade was first measured. The axial load and removal ratio of the scraper were then compared among burrs, discrete cement blocks with three spacings, and continuous cement rings with three thicknesses. For 25 structural parameter combinations, the average scraping force, material failure volume, and scraping work were analyzed, and the schemes were screened by range analysis and equal-weight comprehensive scoring. The results show that the equivalent stiffness of the spring assembly is about 120.9 N/mm. When the cement block spacing increases from 100 mm to 200 mm, the cumulative scraping work decreases by 52.48%. When the continuous cement ring thickness increases from 6 mm to 8 mm, the cumulative scraping work increases by 36.74%; under the 10 mm condition, the peak load reaches 180 kN and the operation is suspended. The orthogonal results show that the blade body length dominates the average scraping force and scraping work, while the cutter wing height dominates the failure volume. Among the 25 schemes, T20 ranks first with a comprehensive score of 0.9492. This study provides a quantitative basis for optimizing scraper blade parameters.

## Keywords

Casing Scraper, Scraping Performance, Numerical Simulation, Orthogonal Optimization

## 1. Introduction

During oil and gas well completion and workover, residual cement, metal burrs, and other deposits on the casing inner wall can reduce the effective drift diameter, hinder downhole operations, impair packer sealing, and cause tool sticking. Zhang *et al.* emphasized the importance of removing residual bridge plug debris and sand in shale gas horizontal wells [1], while Lei *et al.* evaluated a negative-pressure wellbore cleaning tool through numerical simulations and laboratory tests [2]. Kiran *et al.* reviewed the causes of well integrity failure [3], and Vralstad *et al.* highlighted the importance of long-term well barrier integrity [4]. Spring-loaded casing scrapers remove deposits through contact, compression, and shearing, with spring-supported blades adapting to variations in casing diameter. However, thick continuous cement attachments may cause excessive scraping resistance, energy consumption, and casing damage. Therefore, understanding the scraping mechanism and the influence of structural parameters is essential for improving removal efficiency.

Previous studies have investigated cement integrity, casing wear, material cutting, and damage modeling. Skorpa and Vralstad examined fluid migration through cement cracks and micro-annuli [5], while Osman *et al.* and Yu *et al.* investigated casing wear under different contact conditions [6] [7]. Bois *et al.* developed a mechanistic model for cement sheath integrity [8]. Regarding cutting mechanics, Ulm and James characterized the mechanical properties of oil well cement using scratch tests [9], Teale introduced the concept of specific cutting energy [10], and Detournay and Defourny established a cutting model incorporating friction [11]. Subsequent studies explored the relationships between rock strength and cutting response [12], cutting depth and failure modes [13], cutting forces and fragmentation [14], and the effects of cutting and frictional contact on drilling performance [15]. For material damage simulation, Hillerborg *et al.* proposed a fracture-based cracking model [16], Lubliner *et al.* developed a concrete plastic-damage model [17], Lee and Fenves incorporated damage-induced stiffness degradation [18], and Grassl and Jirasek established a coupled damage-plasticity model [19]. Although these studies provide a theoretical basis, limited research has addressed the mechanical scraping of cement attachments on casing inner walls, particularly the influence of scraper structural parameters on removal resistance, efficiency, and energy consumption.

In summary, although wellbore cleaning, contact wear, material cutting, and numerical simulation have been widely studied, the relationship between the structural parameters of spring-loaded casing scrapers and their obstacle-removal performance remains unclear. Discrete cement blocks and continuous cement rings differ in contact and failure characteristics, so a single indicator, such as scraping force or removal amount alone, cannot fully evaluate tool performance. This paper therefore takes a 7-inch mandrel rotary spring scraper as the research object and combines laboratory tests with finite element simulation. Spring compression tests and bench obstacle-removal tests under different attachment con-

ditions are first conducted to obtain the scraping load, cumulative scraping work, and removal effect. A finite element model is then built. An L25($5^5$) orthogonal design is used to examine how five parameters, namely blade side inclination angle, cutter wing spacing, cutter wing height, body length, and spring equivalent parameters, affect the average scraping force, material failure volume, and scraping work. Range analysis and comprehensive evaluation are applied to screen reasonable parameter combinations. By combining laboratory tests with numerical orthogonal optimization, this work establishes a comprehensive evaluation approach covering scraping resistance, material removal capability, and energy consumption, which provides a reference for the structural optimization of spring-loaded casing scrapers.

## 2. Experiments

### 2.1. Test Setup and Scheme

The tests were conducted using a 7-inch mandrel-type rotary spring-compensated casing scraper with an overall length of 2172 mm. The scraper consisted of 12 blades arranged in four groups, with eight springs beneath each blade, and had a working diameter of 146 - 168 mm. The P110 casing specimen was approximately 2 m long, with an inner diameter of 152.5 mm. The test simulator was 13 m high, with an effective stroke of 3.7 m, a rated weight on bit of 20 t, a maximum rotational speed of 83 r/min, and a rated torque of 20,000 N·m. In the spring compression tests, the eight-spring assembly beneath a single blade was compressed to 11 mm at loading rates of 5, 10, and 25 mm/min, with three repetitions at each rate. The scraping tests included metal burrs, discrete cement blocks with a thickness of 8 mm and spacings of 100, 150, and 200 mm, and continuous cement rings with thicknesses of 6, 8, and 10 mm. The cement specimens were prepared using API Class G oil-well cement at a water-cement ratio of 0.40 and cured for 7 days at 20 ± 2 °C and a relative humidity of at least 95%. The scraping tests were performed at an axial feed rate of 300 mm/min and a rotational speed of 30 r/min, with three independent specimens for each condition. Axial force and displacement data were synchronously recorded at a sampling frequency of at least 100 Hz. A 250 mm unobstructed lead-in section was provided before each specimen. The position of initial contact between the scraper and the obstacle was defined as the displacement origin, and axial force and displacement data were recorded over an effective scraping travel of 0 - 1400 mm, excluding the lead-in section.

Axial scraping work excludes rotary work and is calculated from resisting axial force $R_z$ in N and travel s in mm:

$$W_z\left[J\right]=10^{-3}\int_{s_0}^{s_1}R_z\left(s\right)\mathrm{d}s \tag{1}$$

where $W_z$ is the axial scraping work, $J$; $R_z$(s) is the axial resistance as a function of axial displacement, $N$; and $S_0$ and $S_1$ are the initial and final positions of integration, respectively, mm.

## 2.2. Test Results

### 2.2.1. Equivalent Spring Stiffness

To study the mechanical response of the blade springs at different compression rates, the loads at different compression displacements were recorded. The results under the same conditions were averaged, and the influence of compression rate on the bearing characteristics and equivalent stiffness of the springs was analyzed.

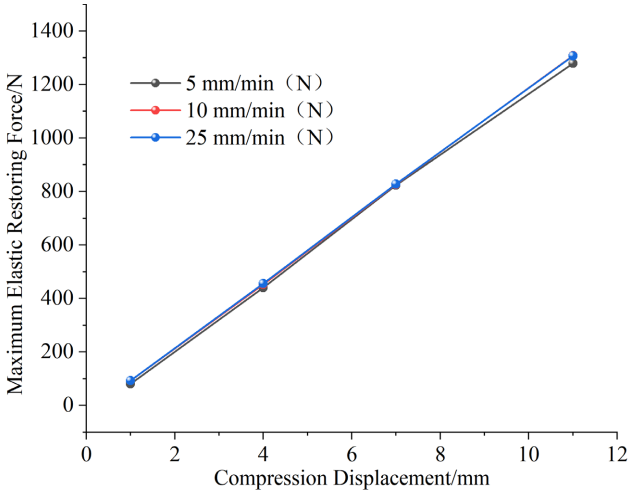



**Figure 1.** Load-displacement curves of the blade spring assembly at different loading rates.

As shown in **Figure 1**, the average load at each rate increases nearly linearly with compression displacement. At the 11 mm stroke, the average loads at 5, 10, and 25 mm/min are 1279.33, 1307.67, and 1307.00 N, respectively. The values at 10 and 25 mm/min differ by less than 0.1% and are 2.2% higher than that at 5 mm/min. The corresponding equivalent stiffness is about 119.0 N/mm at 5 mm/min, and 120.9 and 120.8 N/mm at 10 and 25 mm/min, respectively. Except for slight fluctuations in the three groups at 5 mm/min, the equivalent stiffness remains stable at about 120.9 N/mm, showing good mechanical consistency.

The maximum working stroke of the spring is about 11 mm, and the measured load-displacement curve conforms to Hooke's law within the elastic range, showing good linear response characteristics. In the full-stroke loading test, the spring showed no plastic deformation or curvature inflection point, indicating that its stress always remained within the elastic limit, the probability of failure is low, and the test results are highly reliable.

### 2.2.2. Load Response to Different Obstacle Morphologies

As shown in **Figure 2**, the peak load is the smallest when the attachment is burrs, at 1.66 kN. When the spacing of discrete cement blocks is 100, 150, and 200 mm, the peak loads are 11.27, 9.26, and 6.36 kN, respectively. When the spacing increases from 100 mm to 200 mm, the peak value decreases by 43.57%. This difference is related to the number of contacts per unit length, single local fragmentation, and cutter re-engagement; however, the number of cement blocks also varies

with spacing, so the load difference cannot be entirely attributed to spacing.

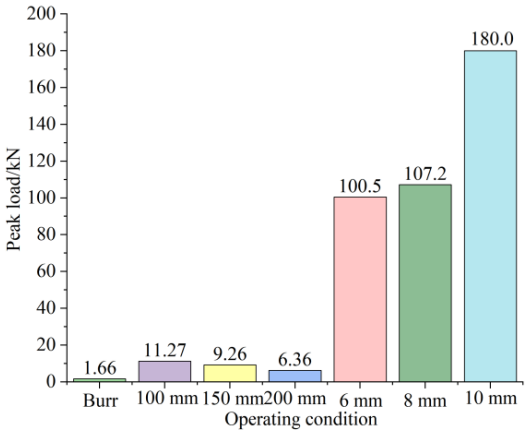



**Figure 2.** Axial peak load under different attachment conditions.

Continuous cement rings produce much higher resistance than discrete cement blocks. At thicknesses of 6 and 8 mm, the peak loads are about 100.5 and 107.2 kN, respectively, i.e., 8.92 and 9.51 times the peak value of the discrete block condition at 100 mm spacing. Unlike discrete blocks, which can be peeled off by local shearing, a continuous annular layer forms a relatively complete obstructed contact zone in both the circumferential and axial directions. The blade therefore stays in contact with the cement longer, and debris extrusion, local crushing, and friction may jointly raise the axial load. At a thickness of 10 mm, the axial resistance rose to 180 kN, reached the upper limit of the instrument, and the test was stopped before full-section removal was completed. The 6 and 8 mm conditions were completed, while the 10 mm condition was not. Therefore, 8 - 10 mm should be regarded as a transition interval that needs further verification under the present bench and specimen conditions, rather than a universal limit thickness for all well conditions.

#### 2.2.3. Cumulative Scraping Work and Removal Ratio (Table 1)

Scraping work is a key indicator of obstacle-removal energy consumption and is jointly affected by axial load, attachment distribution, and scraping stroke. As shown in **Figure 3**, the cumulative scraping work decreases markedly as the cement block spacing increases. At spacings of 100, 150, and 200 mm, the cumulative scraping work is 8.821, 5.962, and 4.192 kJ, respectively. Increasing the spacing from 100 to 150 mm reduces the work by 32.41%, and further increasing it to 200 mm reduces it by another 29.69%, i.e., 52.48% lower than the 100 mm condition in total. The reason is that a larger spacing means fewer attachments per unit length and hence less frequent extrusion, shearing, and crushing between the blades and the blocks. The removed cement masses in the three conditions are 997.5, 662.4, and 605.0 g, corresponding to an energy consumption per unit mass of 8.84, 9.00, and 6.93 kJ/kg. The 200 mm condition is 21.65%

lower than the 100 mm condition, while the 150 mm condition is slightly higher, so the energy consumption per unit mass does not decrease monotonically with spacing. Thus, the reduction of cumulative scraping work depends not only on the total amount of attachments but also on their distribution and the local crushing process.

**Table 1.** Scraping work and variability under different conditions.

| Scraping condition | Scraping work (kJ) | Standard deviation (kJ) | CV (%) |
|---|---|---|---|
| Burr | 1.062 | 0.049 | 4.6 |
| 100 mm spacing | 8.821 | 0.335 | 3.8 |
| 150 mm spaci | 5.962 | 0.304 | 5.1 |
| 200 mm spaci | 4.192 | 0.184 | 4.4 |
| 6 mm | 82.987 | 5.145 | 6.2 |
| 8 mm | 113.473 | 6.354 | 5.6 |
| 10 mm | 148.447 | 10.836 | 7.3 |

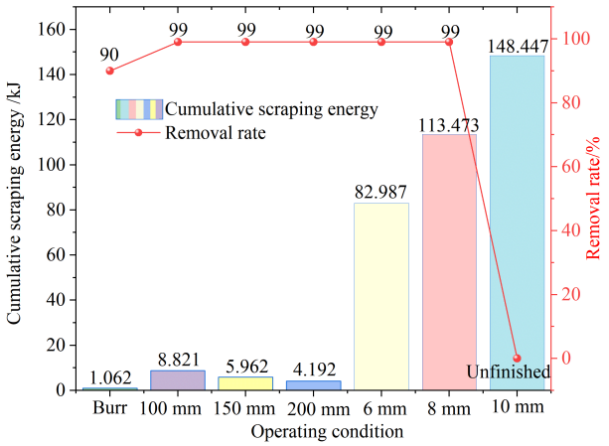



**Figure 3.** Cumulative scraping work and removal ratio under different obstacle conditions.

Continuous cement rings require much more scraping work than discrete cement blocks. At thicknesses of 6, 8, and 10 mm, the cumulative scraping work is 82.987, 113.473, and 148.447 kJ, respectively, with the 8 mm condition 36.74% higher than the 6 mm condition. Thicker rings intensify the contact and crushing between the blades and the cement, which markedly raises the energy consumption. At 10 mm, although full-section scraping was not completed, the recorded cumulative work was still 30.82% higher than that of the 8 mm condition, reflecting severe high-resistance energy consumption under thick ring conditions. However, because the effective scraping strokes differ, a nonlinear energy growth relationship at equal stroke cannot be established directly from these data.

In terms of removal effect, the burr condition consumed only 1.062 kJ of cumulative work and achieved a cross-sectional removal ratio of about 90%. For the three block conditions with spacings of 100, 150, and 200 mm, the cumulative

work ranged from 4.192 to 8.821 kJ, and the removal ratio reached about 99% in all cases. The 6 and 8 mm cement rings also achieved about 99% removal, but at a much higher cost of 82.987 and 113.473 kJ, respectively. This indicates that once the obstacle changes from discrete to continuous distribution, far more mechanical work is needed for a similar removal effect. At a thickness of 10 mm, the excessive axial resistance suspended the operation, and full-section removal could not be guaranteed.

In summary, the scraper has the characteristics of low energy consumption and high removal ratio for discrete obstacles, while continuous thick cement rings significantly increase scraping resistance and energy consumption, and may even cause sticking. Therefore, reducing scraping resistance and cumulative scraping work while ensuring the removal effect is the key objective of scraper structural optimization.

## 3. Numerical Simulation

### 3.1. Geometric Modeling and Mesh Generation

Based on the geometric design parameters of the scraper, a fully parameterized three-dimensional finite element model consisting of the blade and the cement-lined pipe was built. The blade material is 20CrNiMo alloy structural steel, with a Young's modulus of 210 GPa, a Poisson's ratio of 0.3, and a density of 7850 kg/m$^3$ [20]. The cement ring material is API Class G high-sulfate-resistant oil well cement. According to uniaxial compression tests, its Young's modulus, Poisson's ratio, and density are taken as 30 GPa, 0.2, and 2400 kg/m$^3$, respectively [21].

The blade was modeled as a rigid body and meshed with tetrahedral elements using the free meshing technique to accommodate its complex geometry. The cement semi-ring was modeled as a deformable body and meshed with hexahedral elements using the sweep meshing technique to better capture the stress distribution and local failure under compression and shear. This meshing strategy balanced geometric adaptability and computational efficiency, as shown in **Figure 4**.

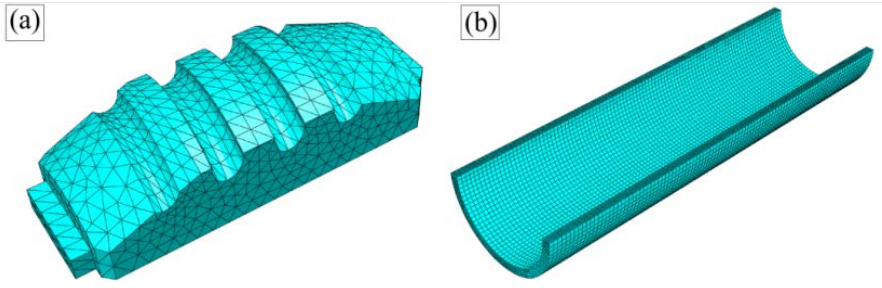



Figure 4. Mesh generation: (a) scraper mesh; (b) cement ring mesh.

The cement material was modeled using the Concrete Damaged Plasticity (CDP) model to describe its nonlinear mechanical behavior under scraping loads through plastic deformation and stiffness degradation. The specific parameters are listed in **Table 2**.

**Table 2.** Concrete damaged plasticity (CDP) model.

| Compressive yield strength/MPa | Compressive strength/MPa | Tensile strength/MPa | Dilation angle | Eccentricity | Fracture energy/(N/m) | $K_c$ |
|---|---|---|---|---|---|---|
| 19.8 | 23.6 | 1.65 | 30 | 0.1 | 25 | 0.667 |

To characterize the nonlinear response of cement material under scraping loads, the concrete damaged plasticity (CDP) model was adopted to describe tensile cracking, compressive plastic deformation, and stiffness degradation. The compressive constitutive behavior was defined using a piecewise linear stress-inelastic strain relationship, with a compressive yield strength of 19.8 MPa and a peak compressive strength of 23.6 MPa. Post-peak stiffness degradation was characterized by the compressive damage variable. Tensile softening was described using a fracture energy-based linear stress-cracking displacement relationship, with a tensile strength of 1.65 MPa and a fracture energy of 25 N/m, corresponding to a complete cracking displacement of 0.0303 mm. Material failure was characterized by tensile cracking displacement and compressive inelastic strain criteria. Once a material point reached the corresponding failure criterion, its load-bearing capacity was considered to be lost, and element deletion was employed to simulate localized crushing and detachment of the cement material. The tensile and compressive damage variables were used to characterize stiffness degradation during cracking and crushing, respectively, while element deletion following material failure was used to represent the numerical removal of cement material.

### 3.2. Boundary Conditions and Load Settings

The outer surface of the cement ring was fully fixed to simulate consolidation on the casing inner wall, as shown in **Figure 5(a)**. An axial displacement load was applied to the scraper to reproduce its advancement, and a reverse friction force was applied on the contact surface to represent the radial force provided by the equivalent spring stiffness. The analysis step time was set to 1 s, and the effective scraping period was about 0 - 0.52 s. After that, the blade separates from the cement ring and the simulated data turn negative, so they were excluded from the calculation.

The spring-loaded casing scraper generates radial support force through the compression of springs beneath the blades, thereby affecting the contact load between the blades and the cement deposits. According to the spring compression tests, the equivalent stiffness of the eight-spring assembly beneath a single blade was 120.9 N/mm. Within the linear elastic range, the radial support force is determined by the initial preload and the elastic restoring force generated by additional radial compression of the blade, expressed as $F_n = F_0 + k_{eq}\delta$, where $F_0$ is the initial preload, $k_{eq}$ is the equivalent stiffness of the spring assembly, and $\delta$ is the additional radial compression displacement. When sliding occurs at the contact interface, the tangential friction force follows Coulomb's friction law, $F_f = \mu F_n$, where $\mu$ is the friction coefficient. The spring stiffness affects the tangential frictional resistance by changing the radial contact load. For the simplified model considering only axial

motion, the corresponding tangential friction force can be used to represent the frictional resistance induced by the spring-generated contact pressure.

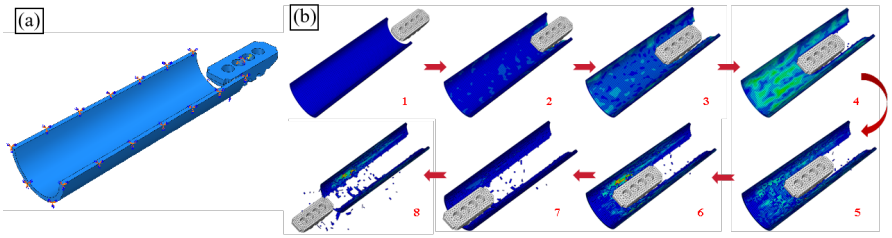



**Figure 5.** (a) Boundary conditions; (b) Demonstration of the scraping process.

As shown in **Figure 5(b)**, after the blade enters the cement, the local contact area gradually expands, stress concentration appears near the contact, and the cement material undergoes local crushing and gradually detaches. As the blade continues to advance, debris and void regions increase, and a continuous scraping channel is finally formed. This process shows that scraping is the result of the combined action of extrusion, shearing, and local fracture.

Considering that the actual casing scraper consists of 12 blades arranged in four groups, with differences in contact positions and interactions among the blades during scraping, a simplified single-blade-semicircular cement ring model was established to investigate local contact behavior, material fracture, and the effects of structural parameters on scraping performance. Since the overall scraping load is also influenced by multiple-blade interactions, repeated cement fracture, and contact friction, the force obtained from the single-blade model cannot be directly multiplied by 12 to represent the total load of the complete scraper. Therefore, the bench tests were primarily used to evaluate the load and energy consumption characteristics during actual obstacle removal, while the numerical simulations were employed to compare the relative performance of different blade configurations under identical boundary conditions, providing a basis for structural parameter optimization.

### 3.3. Orthogonal Simulation Experiment Design

To clarify how the blade structural parameters affect scraping performance, five orthogonal test factors were selected based on the scraper structure and the blade-cement contact characteristics. They are side inclination angle A, cutter wing spacing B, cutter wing height C, blade body length D, and spring equivalent stiffness E. The side inclination angle mainly governs the cutting force direction; the cutter wing spacing affects the contact distribution on the cement; the cutter wing height affects local extrusion and crushing; the body length determines the scraping contact range; and the spring stiffness reflects the radial pressing force. Five levels were set for each factor within its design range: A = 20 - 40 degrees, B = 22 - 42 mm, C = 8 - 16 mm, D = 156 - 196 mm, and E = 100 - 140 N/mm. Because a full factorial test would be too costly, an L25($5^5$) orthogonal design with 25 simulation conditions was adopted. The average scraping force, material failure vol-

ume, and scraping work were used as evaluation indicators. Range analysis was applied to rank the influence of each factor, and comprehensive scoring was used to screen reasonable parameter combinations.

### 3.4. Orthogonal Test Results and Stress Contours

Following the L25($5^5$) orthogonal design, finite element simulations were performed for the 25 parameter combinations. The average scraping force, material failure volume, and scraping work of each condition were extracted, and a comprehensive score was calculated to evaluate the effect of each combination on scraping performance. The results are summarized in **Table 3**.

**Table 3.** Summary of orthogonal simulation results.

| Test No. | A/(˚) | B/mm | C/mm | D/mm | E/(N/mm) | Y1 Scraping force F/N | Y2 Failure volume V/mm$^3$ | Y3 Scraping work W/J | Y (comprehensive) |
|---|---|---|---|---|---|---|---|---|---|
| T1 | 20 | 22 | 8 | 156 | 100 | 2641.9 | 411,788 | 893.332 | 0.4890 |
| T2 | 20 | 27 | 10 | 166 | 110 | 2989.0 | 436,789 | 995.976 | 0.3391 |
| T3 | 20 | 32 | 12 | 176 | 120 | 3173.0 | 443,298 | 999.883 | 0.3152 |
| T4 | 20 | 37 | 14 | 186 | 130 | 3225.5 | 434,065 | 999.223 | 0.2306 |
| T5 | 20 | 42 | 16 | 196 | 140 | 3415.1 | 422,772 | 988.140 | 0.1052 |
| T6 | 25 | 22 | 10 | 176 | 130 | 3047.3 | 440,502 | 998.931 | 0.3400 |
| T7 | 25 | 27 | 12 | 186 | 140 | 3069.7 | 434,912 | 974.982 | 0.3411 |
| T8 | 25 | 32 | 14 | 196 | 100 | 3204.0 | 416,978 | 998.966 | 0.1130 |
| T9 | 25 | 37 | 16 | 156 | 110 | 2606.4 | 417,422 | 884.605 | 0.5609 |
| T10 | 25 | 42 | 8 | 166 | 120 | 2795.0 | 446,679 | 903.918 | 0.6705 |
| T11 | 30 | 22 | 12 | 196 | 110 | 3117.0 | 438,492 | 997.571 | 0.3040 |
| T12 | 30 | 27 | 14 | 156 | 120 | 2450.3 | 434,516 | 873.310 | 0.7639 |
| T13 | 30 | 32 | 16 | 166 | 130 | 2598.7 | 423,251 | 867.518 | 0.6420 |
| T14 | 30 | 37 | 8 | 176 | 140 | 2809.5 | 457,033 | 963.132 | 0.6182 |
| T15 | 30 | 42 | 10 | 186 | 100 | 3022.3 | 457,150 | 991.008 | 0.4875 |
| T16 | 35 | 22 | 14 | 166 | 140 | 2551.1 | 437,462 | 889.757 | 0.7165 |
| T17 | 35 | 27 | 16 | 176 | 100 | 2508.8 | 426,528 | 910.077 | 0.6085 |
| T18 | 35 | 32 | 8 | 186 | 110 | 2839.8 | 452,352 | 967.393 | 0.5645 |
| T19 | 35 | 37 | 10 | 196 | 120 | 2772.2 | 455,062 | 997.464 | 0.5452 |
| T20 | 35 | 42 | 12 | 156 | 130 | 2488.1 | 452,010 | 839.819 | 0.9492 |
| T21 | 40 | 22 | 16 | 186 | 120 | 2790.5 | 431,872 | 960.168 | 0.4461 |
| T22 | 40 | 27 | 8 | 196 | 130 | 3117.7 | 446,501 | 997.268 | 0.3633 |
| T23 | 40 | 32 | 10 | 156 | 140 | 2712.6 | 450,830 | 857.418 | 0.8263 |
| T24 | 40 | 37 | 12 | 166 | 100 | 2553.6 | 443,416 | 890.985 | 0.7568 |
| T25 | 40 | 42 | 14 | 176 | 110 | 2880.2 | 437,621 | 951.306 | 0.4758 |

Note: 1. Y1 is the average scraping force, Y2 is the failure volume, and Y3 is the scraping work; 2. The spring stiffness is applied in the form of friction force in the simulation settings.

To quantitatively evaluate the cement crushing performance of different blade configurations, the failed material volume was adopted as an indicator of material removal capability. In the numerical simulations, deleted cement elements were identified based on their element status, and their initial volumes were summed to obtain the cement failure volume under each operating condition. The failed volume was calculated as follows:

$$V_f = \sum_{e=1}^{N} V_{e0} \left(1 - \mathrm{STATUS}_e\right) \tag{2}$$

where $V_f$ is the failed cement volume ($mm^3$); $N$ is the total number of cement elements; $V_{e0}$ is the initial volume of the $e$-th element ($mm^3$); and $\mathrm{STATUS}_e$ is the element status variable, where 1 indicates an active element and 0 indicates a deleted element.

Based on this method, the failed cement volumes for the 25 orthogonal simulation cases were calculated. These results, together with the average scraping force and axial scraping work, were used to evaluate the effects of blade structural parameters on cement crushing and scraping performance. The calculated failed cement volumes ranged from 411,788 to 457,150 $mm^3$, indicating differences in the numerically predicted material removal among different combinations of blade structural parameters.

### 3.5. Range Analysis and Preferred Scheme

For each factor, the mean response at each level was calculated from its five runs; the range R is the difference between the maximum and minimum level means. A larger R denotes greater sensitivity within the tested levels. The ranking results for F, V, W, and the composite score Y are summarized below.

For average force, the sensitivity order was D > A > B > E > C. The mean force increased from 2579.86 to 3125.20 N when D increased from 156 to 196 mm (21.14%). Thus, reducing blade length is favorable for lowering force over the tested range. For failure volume, the order was C > A > B > E > D. Cutter-wing height C produced the largest range (23697.6 $mm^3$); increasing height from 10 to 16 mm reduced the corresponding mean removed volume from 448066.6 to 424369.0 $mm^3$. For scraping work, the order was D > A > C > E > B, consistent with the strong influence of blade length on average force. The corresponding D range was 126.185 J. For the equal-weight score, the factor order was D > A > E > B > C. Although the combination suggested by separate level means need not coincide with a tested run, T20 was the best of the 25 simulated schemes: A = 35˚, B = 42 mm, C = 12 mm, D = 156 mm, and E = 130 N/mm. It achieved F = 2488.1 N, V = 452,010 $mm^3$, W = 839.819 J, and S = 0.9492. Experimental validation is still needed before identifying it as an optimal field-ready design.

## 4. Conclusions

In this study, experiments and numerical simulation were combined to analyze the scraping load, removal effect, and energy consumption of the casing scraper

under different attachment conditions. Orthogonal tests were then used to clarify the influence of structural parameters on scraping performance. The main conclusions are as follows:

1) The 8-spring assembly of a single blade exhibits a nearly linear load-displacement response at compression rates of 5 - 25 mm/min. Its equivalent stiffness is about 120.9 and 120.8 N/mm at 10 and 25 mm/min, respectively, which can serve as an experimental reference for blade preload modeling.

2) When the cement block spacing increases from 100 mm to 200 mm, the peak load decreases from 11.27 kN to 6.36 kN, and the cumulative scraping work decreases from 8.821 kJ to 4.192 kJ. Compared with discrete cement blocks, continuous cement rings have higher resistance and energy demand. The cumulative work at thicknesses of 6 and 8 mm is 82.987 and 113.473 kJ, respectively, while the 10 mm condition reaches the 180 kN range limit and is suspended.

3) The orthogonal range analysis shows that the body length D has the most obvious influence on the average scraping force and scraping work, while the cutter wing height C has the greatest influence on the material failure volume. The side inclination angle A also affects multi-indicator performance. Structural optimization should take into account reducing resistance, maintaining removal volume, and reducing power consumption, and should not take the maximum failure volume as the sole criterion.

4) Among the 25 schemes, T20 achieves the highest equal-weight comprehensive score (0.9492), with an average scraping force of 2488.1 N, a failure volume of 452010 $mm^3$, and the lowest scraping work of 839.819 J. T20 is therefore recommended as the preferred scheme for experimental verification.

## Author Contributions

Song Zeng: Conceptualization, methodology, investigation, data analysis, and writing - original draft. Chaoyang Yu: Supervision, and writing - review and editing. Geng Peng: Numerical simulation. Zheng Li: Experimental, data curation. All authors have read and approved the final version of the manuscript.

## Conflicts of Interest

The authors declare no conflicts of interest regarding the publication of this paper.

## References

[1] Zhang, H., Yang, S., Liu, D., Li, Y., Luo, W. and Li, J. (2020) Wellbore Cleaning Technologies for Shale-Gas Horizontal Wells: Difficulties and Countermeasures. *Natural Gas Industry B*, **7**, 190-195. https://doi.org/10.1016/j.ngib.2020.03.003

[2] Lei, Q.L., Wang, X.Q., Tang, G., *et al.* (2020) Simulation and Experimental Study on Fishing Performance of Vacuum Suction Wellbore Cleaning Tool. *Mathematical Problems in Engineering*, **2020**, Article ID: 2371059. https://doi.org/10.1155/2020/2371059

[3] Kiran, R., Teodoriu, C., Dadmohammadi, Y., Nygaard, R., Wood, D., Mokhtari, M., *et al.* (2017) Identification and Evaluation of Well Integrity and Causes of Failure of

Well Integrity Barriers (A Review). *Journal of Natural Gas Science and Engineering*, **45**, 511-526. https://doi.org/10.1016/j.jngse.2017.05.009

[4] Vrålstad, T., Saasen, A., Fjær, E., Øia, T., Ytrehus, J.D. and Khalifeh, M. (2019) Plug & Abandonment of Offshore Wells: Ensuring Long-Term Well Integrity and Cost-Efficiency. *Journal of Petroleum Science and Engineering*, **173**, 478-491. https://doi.org/10.1016/j.petrol.2018.10.049

[5] Skorpa, R. and Vrålstad, T. (2018) Visualization of Fluid Flow through Cracks and Microannuli in Cement Sheaths. *SPE Journal*, **23**, 1067-1074. https://doi.org/10.2118/180019-pa

[6] Osman, O.A., Merah, N., Abdul Samad, M., Baig, M.M.A., Samuel, R., Alshalan, M., *et al.* (2022) Casing Wear and Wear Factors: New Experimental Study and Analysis. *Materials*, **15**, Article 6544. https://doi.org/10.3390/ma15196544

[7] Yu, H., Lian, Z., Lin, T., Liu, Y. and Xu, X. (2016) Experimental and Numerical Study on Casing Wear in Highly Deviated Drilling for Oil and Gas. *Advances in Mechanical Engineering*, **8**, 1-15. https://doi.org/10.1177/1687814016656535

[8] Bois, A., Garnier, A., Galdiolo, G. and Laudet, J. (2012) Use of a Mechanistic Model to Forecast Cement-Sheath Integrity. *SPE Drilling & Completion*, **27**, 303-314. https://doi.org/10.2118/139668-pa

[9] Ulm, F. and James, S. (2011) The Scratch Test for Strength and Fracture Toughness Determination of Oil Well Cements Cured at High Temperature and Pressure. *Cement and Concrete Research*, **41**, 942-946. https://doi.org/10.1016/j.cemconres.2011.04.014

[10] Teale, R. (1965) The Concept of Specific Energy in Rock Drilling. *International Journal of Rock Mechanics and Mining Sciences & Geomechanics Abstracts*, **2**, 57-73. https://doi.org/10.1016/0148-9062(65)90022-7

[11] Detournay, E. and Defourny, P. (1992) A Phenomenological Model for the Drilling Action of Drag Bits. *International Journal of Rock Mechanics and Mining Sciences & Geomechanics Abstracts*, **29**, 13-23. https://doi.org/10.1016/0148-9062(92)91041-3

[12] Richard, T., Dagrain, F., Poyol, E. and Detournay, E. (2012) Rock Strength Determination from Scratch Tests. *Engineering Geology*, **147**, 91-100. https://doi.org/10.1016/j.enggeo.2012.07.011

[13] Zhou, Y. and Lin, J. (2013) On the Critical Failure Mode Transition Depth for Rock Cutting. *International Journal of Rock Mechanics and Mining Sciences*, **62**, 131-137. https://doi.org/10.1016/j.ijrmms.2013.05.004

[14] Jaime, M.C., Zhou, Y., Lin, J. and Gamwo, I.K. (2015) Finite Element Modeling of Rock Cutting and Its Fragmentation Process. *International Journal of Rock Mechanics and Mining Sciences*, **80**, 137-146. https://doi.org/10.1016/j.ijrmms.2015.09.004

[15] Detournay, E., Richard, T. and Shepherd, M. (2008) Drilling Response of Drag Bits: Theory and Experiment. *International Journal of Rock Mechanics and Mining Sciences*, **45**, 1347-1360. https://doi.org/10.1016/j.ijrmms.2008.01.010

[16] Hillerborg, A., Modéer, M. and Petersson, P.-. (1976) Analysis of Crack Formation and Crack Growth in Concrete by Means of Fracture Mechanics and Finite Elements. *Cement and Concrete Research*, **6**, 773-781. https://doi.org/10.1016/0008-8846(76)90007-7

[17] Lubliner, J., Oliver, J., Oller, S. and Oñate, E. (1989) A Plastic-Damage Model for Concrete. *International Journal of Solids and Structures*, **25**, 299-326. https://doi.org/10.1016/0020-7683(89)90050-4

[18] Lee, J. and Fenves, G.L. (1998) Plastic-Damage Model for Cyclic Loading of Concrete

Structures. *Journal of Engineering Mechanics*, **124**, 892-900. https://doi.org/10.1061/(asce)0733-9399(1998)124:8(892)

[19] Grassl, P. and Jirásek, M. (2006) Damage-Plastic Model for Concrete Failure. *International Journal of Solids and Structures*, **43**, 7166-7196. https://doi.org/10.1016/j.ijsolstr.2006.06.032

[20] Meng, W., Wang, H., Ma, H., Zhang, Y. and Yao, L. (2026) Research on the Lubrication and Thermal Effects of Single-Metal Seals on Sealing Performance. *Lubricants*, **14**, Article 47. https://doi.org/10.3390/lubricants14020047

[21] Guner, D., Ozturk, H. and Erkayaoglu, M. (2017) Investigation of the Elastic Material Properties of Class G Cement. *Structural Concrete*, **18**, 84-91. https://doi.org/10.1002/suco.201600020